

Quantum critical dynamics in a spinor Hubbard model quantum simulator

Jared O. Austin¹, Zihe Chen¹, Zachary N. Shaw ¹, Khan W. Mahmud^{2,3} & Yingmei Liu ¹ 

Three-dimensional (3D) strongly correlated many-body systems, especially their dynamics across quantum phase transitions, are prohibitively difficult to be numerically simulated. We experimentally demonstrate that such complex many-body dynamics can be efficiently studied in a 3D spinor Bose-Hubbard model quantum simulator, consisting of antiferromagnetic spinor Bose-Einstein condensates confined in cubic optical lattices. We find dynamics and scaling effects beyond the scope of existing theories at superfluid-insulator quantum phase transitions, and highlight spin populations as a good observable to probe the quantum critical dynamics. Our data indicate that the scaling exponents are independent of the nature of the quantum phase transitions. We also conduct numerical simulations in lower dimensions using time-dependent Gutzwiller approximations, which qualitatively describe our observations.

¹Department of Physics, Oklahoma State University, Stillwater, OK, USA. ²Joint Quantum Institute, University of Maryland, College Park, MD, USA. ³Present address: Quidient LLC, Columbia, MD, USA. email: yingmei.liu@okstate.edu

Physical modeling of three-dimensional (3D) strongly correlated many-body systems, especially their critical dynamics across quantum phase transitions, is a fast-moving research frontier with immediate applications spanning from adiabatic quantum state preparations to developing novel materials^{1–9}. Dynamics of phase transitions have been a rich but challenging research theme. One paradigm of dynamical studies is the Kibble–Zurek mechanism (KZM), which characterizes dynamics into two regimes: the impulse regime, where a system is frozen due to diminished energy gaps and slowed equilibrations in the vicinity of phase transition points, and the adiabatic regime, where a system with considerable energy gaps progresses adiabatically^{9–13}. Impeded by the intrinsic complexity of the many-body systems and limitations of existing numerical techniques, theoretical studies of these systems have been performed mainly in homogeneous systems and lower dimensions^{1–3,14–20}. It has been suggested, however, that such complicated many-body dynamics could be efficiently studied in 3D spinor Bose–Hubbard (BH) model quantum simulators, consisting of antiferromagnetic spinor Bose–Einstein condensates (BECs) in cubic optical lattices^{3,4,6,21}. Possessing spin degrees of freedom and exhibiting magnetic order and superfluidity, these 3D spinor quantum simulators are well-isolated quantum systems that are highly programmable with a remarkable degree of control over many parameters, such as temperature, spin, density, and dimensionality^{3–6,21–24}. When lattice-trapped bosons are suddenly quenched from the superfluid (SF) phase to the Mott-insulator (MI) phase, the BH model is nearly integrable, yielding nonthermal steady states preserving memory of the initial state^{9,14}. Another distinctive and useful feature of these 3D quantum simulators is their ability to tune the nature of SF-MI quantum phase transitions, i.e., spinor gases can cross first-order (second-order) SF-MI transitions when the quadratic Zeeman energy q is smaller (larger) than the spin-dependent interaction energy U_2 in even Mott lobes (see Supplementary Note 2)^{4,5,20–23}. U_2 also enables spin-mixing oscillations among multiple spin components and generates ferromagnetic and antiferromagnetic order along with various magnetic states including spin singlets and nematic states^{4,21–25}. These 3D quantum simulators have thus been suggested as an ideal platform for studying quantum coherence, long-range order, magnetism, quantum phase transitions, and symmetry breaking^{4–6,21,22}.

In this paper, we experimentally demonstrate the strength of 3D spinor BH model quantum simulators and explore the quantum critical dynamics by revealing asymmetric impulse–adiabatic regimes^{16,26} as spinor gases are quenched across SF to spinor MI quantum phase transitions at different speeds. Our observations, going beyond the adiabatic–impulse–adiabatic regimes studied in many publications^{9–13,16,27,28}, confirm the impulse regime is enlarged to cover the entire SF phase and part of the MI phase due to negligible excitations within the SF phase^{16,26}. We find quench dynamics and scaling effects at SF-MI quantum phase transitions, which are outside the framework of existing theories including KZM. The observed power law scaling exponents are independent of the nature of SF-MI transitions. We also compare the dynamics observed using both spin populations and SF order parameters as observables and discuss the benefits and limitations of each. While numerical simulations in 3D multicomponent systems are prohibitively difficult to perform for further verification of our results, we conduct theoretical simulations in 2D and find qualitative agreements with the experiment.

Results and discussion

Each experimental cycle is started with a spin-1 ($F = 1$) sodium spinor BEC at its SF ground state, the longitudinal polar state

where $\rho_0 = 1$ and $m = 0$, at a given q . Here ρ_{m_F} is the fractional population of atoms in the $|F = 1, m_F\rangle$ state, m_F is the magnetic quantum number, and $m = \rho_{-1} + \rho_{+1}$ is the magnetization. The investigated q values are of the same order of magnitude as the spin-dependent interaction U_2 . Spinor gases are characterized as ferromagnetic (antiferromagnetic) when U_2 is negative (positive)^{4,23}. Sodium spinor BECs with $U_2 \simeq 0.035U_0 > 0$ studied in this paper are a good example of antiferromagnetic spinor gases (See Supplementary Note 1)⁶. Here, U_0 is the spin-independent interaction. We load spinor BECs into a cubic lattice by linearly quenching the lattice depth u_L , which results in an exponential increase in the ratio of U_0 to the hopping energy J . Similar to scalar bosons, spinor gases can cross SF-MI transitions when U_0/J becomes larger than critical values^{5,6,20,21,21–23}. We describe the lattice-confined spinor gases with the spin-1 BH Hamiltonian and compute their static and dynamic properties using the Gutzwiller approximation (see “Methods”). Note that the linear Zeeman energy, which remains constant during collisional spin interconversions, can be neglected in the Hamiltonian^{4,21,23}.

Quantum critical dynamics probed via spin populations. Figure 1 compares density profiles of various spin components, derived from numerical simulations in systems similar to the experimental system but in two dimensions (2D), after the lattice depth u_L is quenched from $2E_R$ to $40E_R$ at different speeds v_{ramp} . Here, the unit of v_{ramp} is E_R per millisecond ($E_R \cdot \text{ms}^{-1}$) and E_R is the recoil energy^{5,21}. For slow quenches, Fig. 1a–c, g clearly display the formation of Mott insulating shells and spin structures. Whereas for fast quenches, Fig. 1d–f, h shows persistence of SF type density profiles. Lattice gases studied in this paper are inhomogeneous systems confined by an overall harmonic trap. In these systems, the BH model predicts that SF and MI regions coexist and many Mott lobes are arranged in a wedding-cake structure (see Fig. 1 and Supplementary Note 2). Such inhomogeneous systems have been suggested as good candidates for adiabatic quantum state preparations, because inhomogeneous phase transitions suppress excitations during quenches⁹.

Our experimental data agree with these predictions, as shown by spin dynamic curves in Fig. 2a. During fast quenches, the observed spin-0 population ρ_0 implies that the initial SF state is frozen as the lattice is quenched across predicted SF-MI transition points (shaded gray area in Fig. 2a) and then starts to evolve inside isolated lattice sites in deep lattices. Whereas in sufficiently slow quenches, our data indicate that atoms stay in the instantaneous ground state during the dynamics and enter the MI phase at a critical U_0/J . For intermediate quench speeds, for example the $v_{\text{ramp}} = 7E_R \cdot \text{ms}^{-1}$ curve in Fig. 2a, partial revivals in the spin-0 population may be observed after ρ_0 reaches its minimum value. Such revivals are not found at slow and fast quench speeds (see Fig. 2a). Qualitatively similar results are obtained from our 2D numerical simulations (see Fig. 2b), although it is harder to realize adiabatic phase transitions in lower dimensional systems where more low-energy states are accessible for excitations⁹. Theoretical calculations also predict that the frequency of the periodic revivals is determined by U_2 and q for a fixed atom number n , while the amplitude of the revivals depends on the quench speed v_{ramp} . The physical limitations of our system, however, prevent us from safely observing full periods of the revivals at intermediate v_{ramp} , as well as the minimum ρ_0 in fast quenches ($v_{\text{ramp}} \gtrsim 28E_R \cdot \text{ms}^{-1}$), due to extremely high power requirements on the lattice beams.

We define the length of the impulse regime as the length of the frozen region, where atoms cannot remain in instantaneous ground states and thus stay frozen in their initial states during quenches, and apply a single ρ_0 cut-off value to mark the edge of

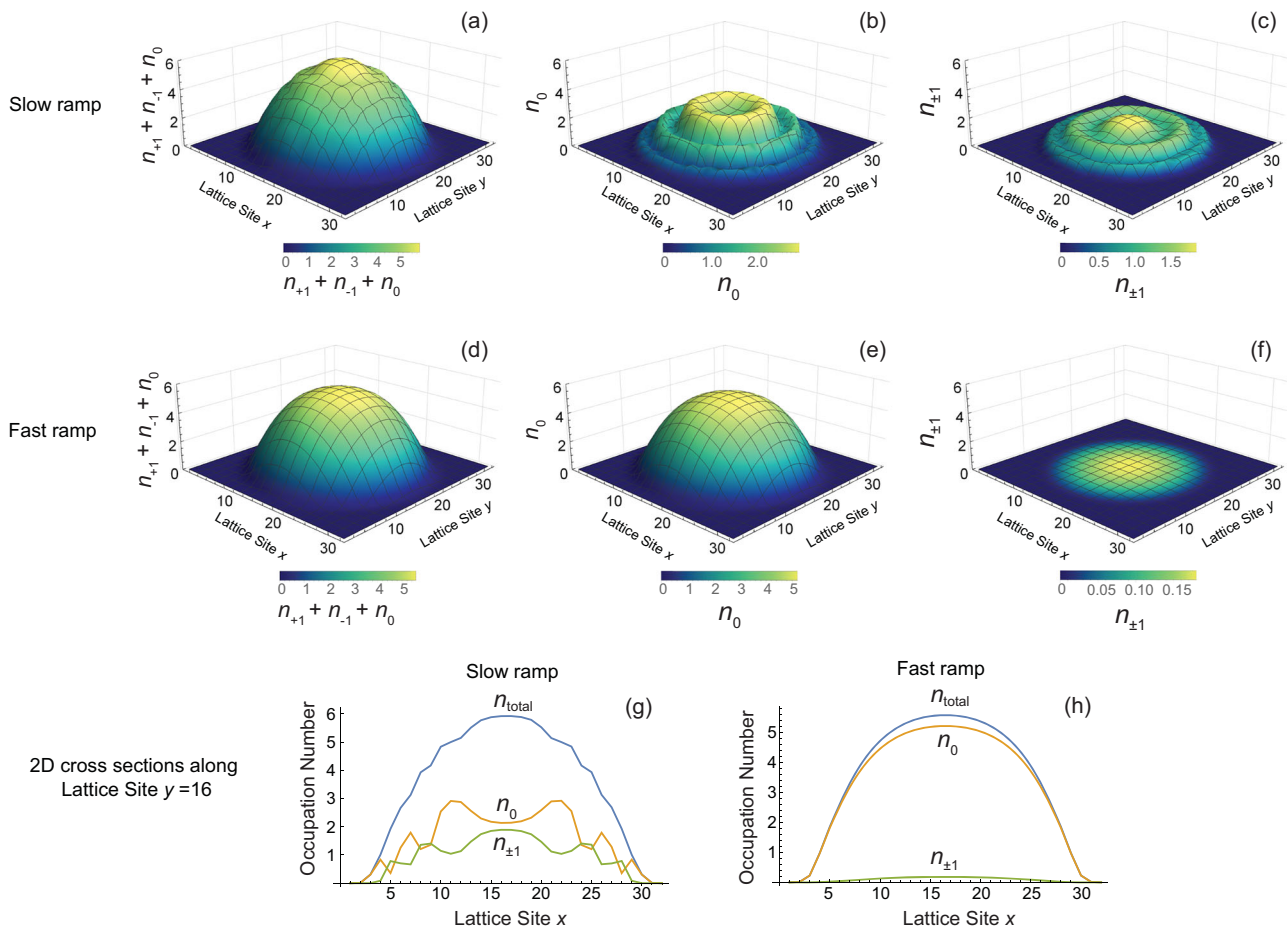


Fig. 1 Predicted density profiles after quenches across quantum phase transitions. **a–c** Predicted density profiles of all atoms, the $m_F = 0$ atoms, and the $m_F = \pm 1$ atoms after a slow quench at the speed $v_{\text{ramp}} = 5E_R \cdot \text{ms}^{-1}$ from a shallow lattice of the depth $u_L = 2E_R$ to a deep lattice at $u_L = 40E_R$, respectively. Here, E_R is the recoil energy, m_F is the magnetic quantum number, and the unit of v_{ramp} is E_R per millisecond ($E_R \cdot \text{ms}^{-1}$). These density profiles are derived from our numerical simulations for 2D lattice-trapped sodium spinor gases of $n_{\text{peak}} = 6$ at $q/h = 42$ Hz using the Bose–Hubbard model and the Gutzwiller approximation (see “Methods”). Here, n_{peak} is the peak occupation number per lattice site, q is the quadratic Zeeman energy, and h is the Planck constant. **d–f** Similar to panels (a–c) but after a fast lattice quench with $v_{\text{ramp}} = 50E_R \cdot \text{ms}^{-1}$. The horizontal axes indicate individual lattice sites along the spatial x -axis and y -axis, respectively. The color scale and vertical axis indicate n , the occupation number per lattice site. **g, h** 2D cross sections of panels (a–c) and panels (d–f) at the 16th lattice site along the y -axis, respectively.

the impulse regime. For example, Fig. 2c is extracted from the observed dynamics by setting the end of the impulse regime at the lattice depth where $\rho_0 = 0.9$. When U_0/J at this lattice depth is plotted against v_{ramp} , two distinct dynamical regions emerge (see Fig. 2c). For relatively slow quenches ($v_{\text{ramp}} \lesssim 13E_R \cdot \text{ms}^{-1}$), the length of the impulse regime does not strongly depend on quench speed. For faster quenches, the length obeys a power law relationship with v_{ramp} as expected from a quantum version of the KZM, although the extracted scaling exponent 1.55(8) is much larger than the 0.67 predicted by a simple KZM for lattice-trapped 3D scalar bosons⁹. We find that the 2D simulations (dashed line in Fig. 2c) and our experimental data are numerically very similar when $v_{\text{ramp}} > 18E_R \cdot \text{ms}^{-1}$ and somewhat similar when $v_{\text{ramp}} \leq 6E_R \cdot \text{ms}^{-1}$, while displaying large discrepancies in the region near the critical ramp speed ($\approx 13E_R \cdot \text{ms}^{-1}$). These discrepancies may be due to the presence of inhomogeneous systems and difference in dimensionality. The scaling exponents extracted from the experiments and the 2D simulations show no strong dependence on the ρ_0 cut-off value as long as the cutoff is sufficiently larger than the minimum observed ρ_0 values. The quenches studied in this paper are exponential in U_0/J , whereas the KZM usually applies to quenches linear in system parameters, so our experiments may have revealed nonuniversal scaling

relations. Our numerical simulations have taken this feature into account, while omitting any finite-temperature or heating effects.

Quantum critical dynamics probed via SF order parameters.

Both ρ_0 and SF order parameters are theoretically good observables for SF-MI phase transitions, due to the similarities in the topology and boundaries of the phase diagrams derived from SF order parameters and ρ_0 when $n > 1$ (see Fig. 2d and Supplementary Note 2). Solid lines in Fig. 2d indicate that ρ_0 in even Mott lobes changes more drastically than in the odd Mott lobes near the SF-MI transition points while within the even Mott lobes the change in ρ_0 gets smaller at higher n . We further analyze these dynamics by examining the SF order parameter, which is proportional to the side peak fraction ϕ measured in experiments. ϕ is a measure of coherence of the wavefunction and is proportional to the number of atoms at zero momentum in the spin-dependent momentum distributions (see “Methods”)^{5,29}. The inset of Fig. 3a illustrates how we extract ϕ . Typical evolutions of ϕ for the three spin components during a quench at an intermediate speed are presented in Fig. 3a. For the spin-0 atoms, ϕ increases steadily until it obtains its maximum around $12E_R$ and then decreases as the lattice gets deeper and the interference pattern disappears. In

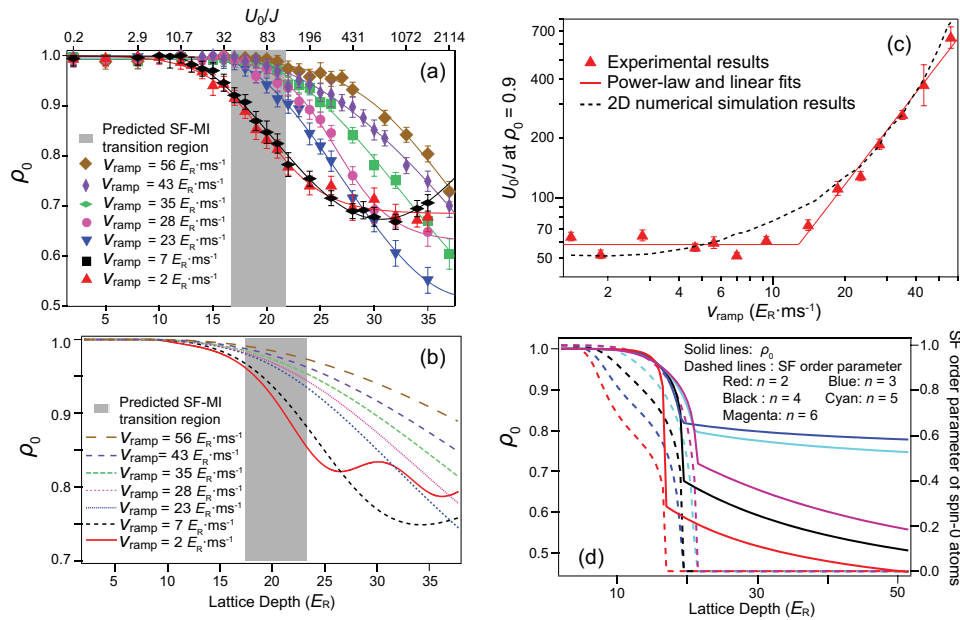


Fig. 2 Quantum critical dynamics probed via spin populations. **a** Observed spin dynamics at various lattice quench speeds v_{ramp} in magnetic fields of $q/h = 42$ Hz. Here, q is the quadratic Zeeman energy, h is the Planck constant, the unit of v_{ramp} is E_R per millisecond ($E_R \cdot \text{ms}^{-1}$), E_R is the recoil energy, and ρ_0 in the figure is the fractional population of the spin-0 component. Solid lines are fitting curves to guide the eye (see “Methods”), and the shaded gray area represents the predicted superfluid to Mott insulator (SF-MI) transition region for the filling factors n of $1 \leq n \leq 6$. The top horizontal axis lists the corresponding U_0/J , where U_0 is the spin-independent interaction energy and J is the hopping energy. **b** Similar to panel **a** but derived from the Bose-Hubbard model for 2D lattice-trapped sodium spinor gases (see “Methods”). **c** Markers correspond to U_0/J extracted from panel **a** at the cutoff of $\rho_0 = 0.9$ as a function of v_{ramp} . The solid line represents a power-law fit of the data in fast quenches and a linear fit in slow quenches. The dashed line is the 2D numerical simulation result. **d** Solid (dashed) lines represent the predicted ρ_0 (the SF order parameter of the spin-0 component) versus the lattice depth u_L after adiabatic ramps in 3D lattice-trapped sodium spinor gases at $q/h = 42$ Hz. Results for a Mott lobe of a certain filling factor n are marked in a given color. The SF order parameter is nonzero (zero) in the SF (MI) phase (see “Methods” and Supplementary Note 2). Error bars represent one standard deviation.

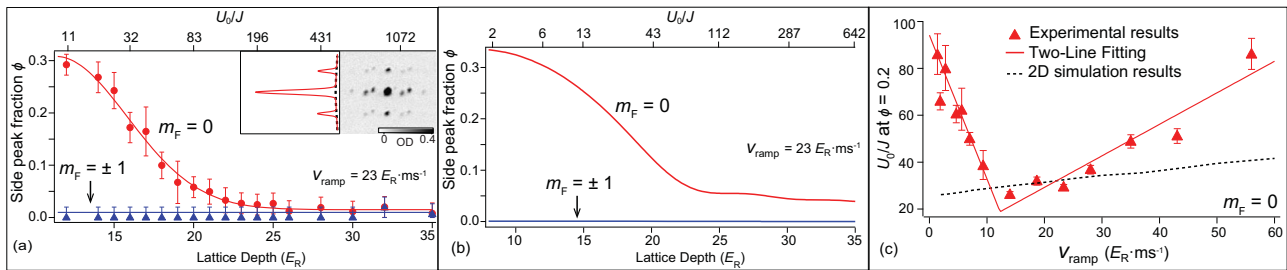


Fig. 3 Quantum critical dynamics probed via superfluid order parameters. **a** Red (blue) markers represent the observed side peak fractions ϕ of the $m_F = 0$ ($m_F = \pm 1$) spin components at $q/h = 42$ Hz during a lattice quench at an intermediate speed, $v_{\text{ramp}} = 23E_R \cdot \text{ms}^{-1}$. Here, q is the quadratic Zeeman energy, h is the Planck constant, E_R is the recoil energy, m_F is the magnetic quantum number, and the unit of v_{ramp} is E_R per millisecond ($E_R \cdot \text{ms}^{-1}$). The red (blue) line is a Gaussian (linear) fit. The top horizontal axis lists the corresponding U_0/J , where U_0 is the spin-independent interaction energy and J is the hopping energy. The inset shows a time-of-flight (TOF) absorption image of the spin-0 atoms and the corresponding density profile of the top, bottom, center peak populations (red line) and of the background population (dashed line) created by integrating along a narrow vertical slice (including only the top, center, and bottom peaks) of the TOF image and by fitting to four Gaussian curves. From these fittings we can extract ϕ by taking the area of the two side peaks and dividing by the total area. The color scale in the TOF image shows the optical density (OD). **b** Similar to panel **a** but derived from the Bose-Hubbard model for 2D lattice-trapped sodium spinor gases (see “Methods”). **c** Markers represent U_0/J , where the measured ϕ of the spin-0 atoms equals 0.2, extracted from curves similar to the one shown in panel **a** but taken at various v_{ramp} . The solid line is a two-line fit and the dashed line represents the 2D numerical simulation results. Error bars represent one standard deviation.

contrast, the observed ϕ for the spin ± 1 components always stays at zero throughout the evolution, which indicates $m_F = \pm 1$ atoms are only formed in the MI phase. These observations agree with our theoretical simulations shown in Fig. 3b.

By defining a cut-off ϕ at which the fitting curve for ϕ of the spin-0 atoms equals 0.2, two different regions again emerge, as shown in Fig. 3c. These regions are divided at roughly the same

critical v_{ramp} ($\approx 13E_R \cdot \text{ms}^{-1}$) as the two regions found in Fig. 2c. For fast (slow) quenches where v_{ramp} is faster (slower) than $13E_R \cdot \text{ms}^{-1}$, Fig. 3c shows that the extracted U_0/J linearly increases (decreases) with v_{ramp} , instead of the power law dependence found in Fig. 2c. This apparent discrepancy together with large disagreements between the numerical simulations and the data (see Fig. 3c) may be due to various reasons. First, spin-0 population ρ_0 is a local

observable for a system confined in a harmonic trap, while the SF order parameter is a global observable that takes into account two-body correlations of all sites by doing a Fourier transform. For a trapped system, it is thus conceivable that the SF order parameter is more affected by noise, temperature and other nonideal situations. Second, because our two-stage microwave imaging method (see “Methods”) is capable of recording both condensed and thermal atoms presented in the optical dipole trap, the measurement of ρ_0 should be much less sensitive to heatings. Nonadiabatic quenches across SF-MI transitions could inherently excite/heat atoms leading to an unavoidable reduction in the visibility of the interference pattern^{30,31}, which may set insurmountable technical limitations for using the SF order parameter as an observable to accurately study the nonadiabatic dynamics. On the other hand, the utilization of spin populations to investigate SF-MI transitions is limited to small q , because these transitions are no longer marked by a significant change in ρ_0 when $q/h > 120$ Hz⁵. Other potential factors that may contribute to the disagreements shown in Fig. 3c include nonequilibrium dynamic and thermalization effects, harmonic trapping effect, and the difference in dimensionality. These coupled with the coexistence of SF and MI regions in inhomogeneous systems make it difficult to compare the impulse regimes derived from SF order parameters across varying quench speeds. Our data indicate that the choice of the cut-off ϕ does not significantly alter the overall observed behavior of the length of the impulse regime, although slopes of the linear fits (solid lines in Fig. 3c) increase as the cutoff value decreases. Another obvious difference from the theoretical predictions for both observables is the observed critical quench speed shown in Fig. 2c and Fig. 3c, which our numerical simulations have not been able to reproduce. The underlying physics of the critical quench speed requires further study, although it could also be due to a dimensional effect, harmonic trapping effect, or experimental peculiarity related to heating effects.

Quantum critical dynamics in different magnetic fields. To test how different local magnetic fields might affect these results, we repeat these experiments at multiple quadratic Zeeman energy q within $0 < q/h < 100$ Hz. We find no significant q dependence in the scaling exponent or the critical v_{ramp} , as shown in Fig. 4. Because $q \ll U_0$, the lack of a significant q dependence is consistent with our theoretical understanding of these transitions. From these experiments, we find the scaling exponent of our system to be 1.6(1) and the critical quench speed at which the impulse regime begins to significantly vary with quench speed to be $13(2)E_R \cdot \text{ms}^{-1}$. Because SF-MI phase transitions are first order in even Mott lobes at $q < U_2 \approx h \times 50$ Hz while second order in odd Mott lobes at any q ^{4,5,20–23}, Fig. 4 implies the scaling exponents are independent of the nature of the SF-MI phase transitions.

Conclusion

In conclusion, we have experimentally demonstrated quench dynamics and scaling effects outside the scope of existing theories in 3D spinor BH model quantum simulators. To explore these dynamics, we have utilized both spin populations and SF order parameters as observables and discuss the technical limitations and benefits of each. Our data indicate the scaling exponents are independent of the nature of SF-MI phase transitions. While it is prohibitively difficult to compute dynamics of multicomponent bosons in 3D lattices, we have performed numerical simulations in lower dimensions and found qualitative agreements with the experiment. This work may indicate the 3D quantum simulators could be more powerful than their classical counterparts, especially in studying many-body quantum dynamics and the

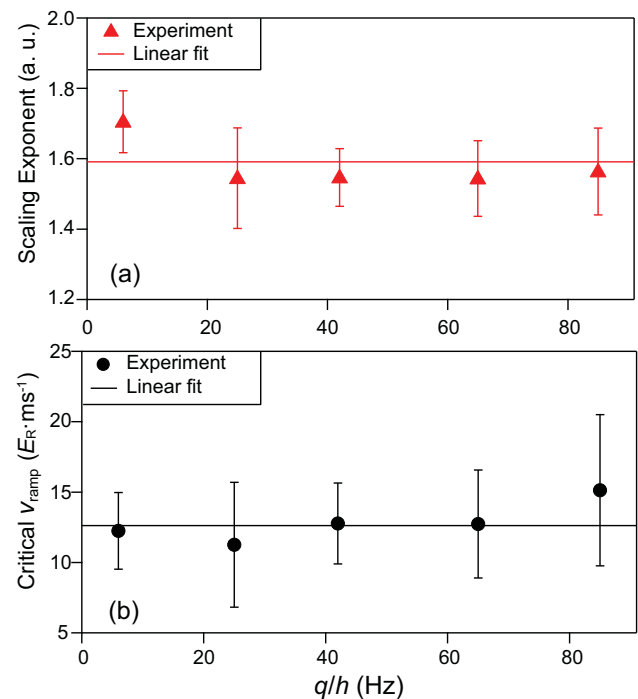


Fig. 4 Quantum critical dynamics in different magnetic fields. a The scaling exponent extracted from the power-law fits as illustrated in Fig. 2c at various quadratic Zeeman energy q . **b** The critical lattice quench speed v_{ramp} at the intersection of the linear and power-law fits shown in Fig. 2c as a function of q . Solid lines are linear fits. Here h is the Planck constant, the unit of v_{ramp} is E_R per millisecond ($E_R \cdot \text{ms}^{-1}$), and E_R is the recoil energy. Symbols correspond to values extracted from fittings over at least eight datasets taken at each q and error bars represent one standard deviation.

interplay of magnetism and superfluidity, although their effectiveness and accuracy is worthy of further study.

Methods

Experimental procedures. Each experimental sequence begins by creating a spin-1 antiferromagnetic spinor BEC containing up to 1.5×10^5 sodium (^{23}Na) atoms in a crossed optical dipole trap of frequencies $\omega_{x,y,z}/2\pi = 132, 132, 197$ Hz at $q/h = 42$ Hz. Here q is the quadratic Zeeman energy and h is the Planck constant. We then apply resonant microwave and imaging pulses to eliminate the atoms in $|F = 1, m_F = \pm 1\rangle$ states. This leaves us with a BEC in its SF ground state, the longitudinal polar state, where $\rho_0 = 1$ and $m = 0$. After the pure state is prepared, we quench q to a desired value using magnetic fields whose strength is tuned within 50 and 600 mG, and then load the BEC into a cubic lattice. The cubic lattice is constructed by three orthogonal standing waves producing a lattice with spacing of 532 nm. The lattice beams originate from a single mode laser at 1064 nm and are frequency shifted by at least 20 MHz from each other. The lattice depth u_L is calibrated using Kapitza–Dirac diffraction patterns. Once loaded we linearly ramp u_L up to the desired value u_L^{final} in a given ramp time (t_{ramp}), which corresponds to a roughly exponential ramp in U_0/J . Here, J is the hopping energy and U_0 is the spin-independent interaction. The atoms are then abruptly released and ballistically expand, before we measure ρ_0 and the SF order parameter with a two-stage microwave imaging method, in which the $m_F = 0$ atoms are pumped up to the $F = 2$ state by resonant microwave pulses for imaging in the first stage and then the $m_F = \pm 1$ atoms are imaged in the second stage^{6,22}. The estimated systematic errors of ρ_0 and the side peak fraction are 0.015 and 0.02, respectively. By holding the lattice ramp speed $v_{\text{ramp}} = u_L^{\text{final}}/t_{\text{ramp}}$ constant while varying the u_L^{final} and t_{ramp} , we produce graphs similar to those found in Fig. 2a and Fig. 3a. Alternatively by varying the holding time after non-adiabatic lattice ramps, spin dynamics can be observed that reveal information about the Fock state distributions and key parameters determining the spinor physics, as demonstrated in our previous work⁶. Each experimental data point represents the average of around 15 shots at a given u_L^{final} and t_{ramp} . Presented error bars correspond to estimated one standard deviation, combined statistical and systematic uncertainties. Each complete set at a given v_{ramp} and q contains 14 or more points at representative u_L^{final} to allow fitting with either a sigmoid function or a piecewise function given by $y = y_0 + A$ if $x \leq x_0$

and $y = y_0 + A \cos(f(x - x_0))$ if $x > x_0$. For the piecewise function, y_0 , A , and x_0 are fitting parameters, while f is held at an appropriate value in order to produce more reliable fittings. The fitting function used for each set was determined by the chi-square of the fitted functions and was then used to calculate the critical lattice depth and its associated error.

Theoretical models. The BH Hamiltonian of lattice-trapped $F = 1$ spinor gases can be expressed as²¹

$$H = -J \sum_{\langle i,j \rangle} (a_{i,m_F}^\dagger a_{j,m_F} + a_{j,m_F}^\dagger a_{i,m_F}) + \frac{U_0}{2} \sum_i \hat{n}_i (\hat{n}_i - 1) + \frac{U_2}{2} \sum_i (\bar{F}_i^2 - 2\hat{n}_i) - \sum_i \mu_i \hat{n}_i + \frac{1}{2} V_T \sum_i (i - L/2)^2 \hat{n}_i + q \sum_i (n_{i,1} + n_{i,-1}), \quad (1)$$

where $\hat{n}_i = \sum_{m_F} a_{i,m_F}^\dagger a_{i,m_F}$ is the total atom number at site- i , $a_{m_F}^\dagger$ (a_{m_F}) are boson creation (destruction) operators with m_F being ± 1 and 0 for spin-1 atoms, the total spin is $\bar{F} = \sum_{m_F, m_F'} a_{m_F}^\dagger \bar{F}_{m_F, m_F'} a_{m_F'}$, the standard spin-1 matrices are $\bar{F}_{m_F, m_F'}$, the spin-dependent interaction is U_2 , the chemical potential is μ , the total number of lattice sites is L , and V_T is the harmonic trap strength. In a mean-field approximation, the above Hamiltonian can be expressed as a sum of independent single site Hamiltonians $H = \sum_i H_i$ with

$$H_i = \frac{U_0}{2} \hat{n}_i (\hat{n}_i - 1) + \frac{U_2}{2} (\bar{F}_i^2 - 2\hat{n}_i) - \mu_i \hat{n}_i - z \sum_{m_F} \psi_{m_F} (a_{i,m_F}^\dagger + a_{i,m_F}) + q \sum_{m_F} m_F^2 n_{i,m_F} + z \sum_{m_F} |\psi_{m_F}|^2. \quad (2)$$

Here z is the number of nearest neighbors, $\psi_{m_F} = \langle a_{i,m_F}^\dagger \rangle = \langle a_{i,m_F} \rangle$ is the SF order parameter, and we absorb the V_T term in the chemical potential. The side peak fraction studied in Fig. 3 is given by $|\langle \hat{a}_{i,m_F} \rangle|^2$ for any site i and is thus proportional to the SF order parameter.

We compute the static and dynamic properties of the spin-1 BH Hamiltonian using the Gutzwiller approximation^{17,20}, which assumes the many-body wave function in the full lattice can be written as a product of local states at L individual sites, $|\Psi_{\text{GW}}\rangle = \prod_{i=1}^L |\phi_i\rangle$ with $|\phi_i\rangle = \sum_{n_{i,m_F}} A_i(n_{i,1}, n_{i,0}, n_{i,-1}) |n_{i,1}, n_{i,0}, n_{i,-1}\rangle$. A_i is the variational parameter at site i . Dynamics are derived from numerically solving the time-dependent Schrödinger equation for specific initial states. To perform the Gutzwiller calculations, we write the matrix elements of the Hamiltonian H_i in the occupation number basis $|n_{i,-1}, n_{i,0}, n_{i,1}\rangle$, and truncate the onsite Hilbert space by allowing a maximum number of particles per site, $n_{\text{max}} = 8$, for which dynamics can be computed efficiently and the truncation effects are negligible.

Data availability

All relevant data of this study are available from the corresponding author upon request.

Received: 6 November 2020; Accepted: 26 February 2021;

Published online: 25 March 2021

References

- Polkovnikov, A., Sengupta, K., Silva, A. & Vengalatorre, M. Nonequilibrium dynamics of closed interacting quantum systems. *Rev. Mod. Phys.* **83**, 863 (2011).
- Braun, S. et al. Emergence of coherence and the dynamics of quantum phase transitions. *Proc. Natl. Acad. Sci. USA* **112**, 3641–3646 (2015).
- Bloch, I., Dalibard, J. & Zwerger, W. Many-body physics with ultracold gases. *Rev. Mod. Phys.* **80**, 885 (2008).
- Stamper-Kurn, D. M. & Ueda, M. Spinor Bose gases: symmetries, magnetism, and quantum dynamics. *Rev. Mod. Phys.* **85**, 1191 (2013).
- Jiang, J. et al. First-order superfluid-to-Mott-insulator phase transitions in spinor condensates. *Phys. Rev. A* **93**, 063607 (2016). and the references therein.
- Chen, Z. et al. Quantum quench and nonequilibrium dynamics in lattice-confined spinor condensates. *Phys. Rev. Lett.* **123**, 113002 (2019).
- Chen, D., White, M., Borries, C. & DeMarco, B. Quantum quench of an atomic Mott insulator. *Phys. Rev. Lett.* **106**, 235304 (2011).
- Lewenstein, M. et al. Ultracold atomic gases in optical lattices: mimicking condensed matter physics and beyond. *Adv. Phys.* **56**, 243 (2007).
- Dziarmaga, J. Dynamics of a quantum phase transition and relaxation to a steady state. *Adv. Phys.* **59**, 1063–1189 (2010).
- Kibble, W. B. Topology of cosmic domains and strings. *J. Phys. A* **9**, 1387 (1976).

- Zurek, W. H. et al. Cosmological experiments in superfluid helium. *Nature* **317**, 505 (1985).
- Zurek, W. H., Dorner, U. & Zoller, P. Dynamics of a quantum phase transition. *Phys. Rev. Lett.* **95**, 105701 (2005).
- Dziarmaga, J., Meisner, J. & Zurek, W. H. Winding up of the wave-function phase by an insulator-to-superfluid transition in a ring of coupled Bose-Einstein condensates. *Phys. Rev. Lett.* **101**, 115701 (2008).
- Roux, G. Quenches in quantum many-body systems: one-dimensional Bose-Hubbard model reexamined. *Phys. Rev. A* **79**, 021608(R) (2009).
- Shimizu, K., Kuno, Y., Hirano, T. & Ichinose, I. Dynamics of a quantum phase transition in the Bose-Hubbard model: Kibble-Zurek mechanism and beyond. *Phys. Rev. A* **97**, 033626 (2018).
- Gardas, B., Dziarmaga, J. & Zurek, W. H. Dynamics of the quantum phase transition in the one-dimensional Bose-Hubbard model: excitations and correlations induced by a quench. *Phys. Rev. B* **95**, 104306 (2017).
- Yamashita, M. & Jack, M. W. Spin structures of spin-1 bosonic atoms trapped in an optical lattice with harmonic confinement. *Phys. Rev. A* **76**, 023606 (2007).
- Batrouni, G. G., Rousseau, V. G. & Scalettar, R. T. Magnetic and superfluid transitions in the one-dimensional spin-1 Boson Hubbard Model. *Phys. Rev. Lett.* **102**, 140402 (2009).
- Clark, S. R. & Jaksch, D. Dynamics of the superfluid to Mott-insulator transition in one dimension. *Phys. Rev. A* **70**, 043612 (2004).
- Natu, S. S., Poxley, J. H. & Das Sarma, S. Static and dynamic properties of interacting spin-1 bosons in an optical lattice. *Phys. Rev. A* **91**, 043620 (2015).
- Mahmud, K. W. & Tiesinga, E. Dynamics of spin-1 bosons in an optical lattice: spin mixing, quantum-phase-revival spectroscopy, and effective three-body interactions. *Phys. Rev. A* **88**, 023602 (2013).
- Zhao, L., Tang, T., Chen, Z., and Liu, Y. Lattice-induced rapid formation of spin singlets in spin-1 spinor condensates. Preprint at <https://arxiv.org/abs/1801.00773> (2018).
- Imambekov, A., Lukin, M. & Demler, E. Spin-exchange interactions of spin-one bosons in optical lattices: singlet, nematic, and dimerized phases. *Phys. Rev. A* **68**, 063602 (2003).
- Ho, T. L. Spinor Bose condensates in optical traps. *Phys. Rev. Lett.* **81**, 742 (1998).
- Ohmi, T. & Machida, K. Bose-Einstein condensation with internal degrees of freedom in alkali atom gases. *J. Phys. Soc. Japan* **67**, 1822–1825 (1998).
- Schützhold, R., Uhlmann, M., Xu, Y. & Fischer, U. R. Sweeping from the superfluid to the Mott phase in the Bose-Hubbard Model. *Phys. Rev. Lett.* **97**, 200601 (2006).
- Chandran, A., Erez, A., Gubser, S. S. & Sondhi, S. L. Kibble-Zurek problem: universality and the scaling limit. *Phys. Rev. B* **86**, 064304 (2012).
- Roychowdhury, K., Moessner, R., and Das, A. Dynamics and correlations at a quantum phase transition beyond Kibble-Zurek. Preprint at <https://arxiv.org/abs/2004.04162> (2020).
- Chin, J. K. et al. Evidence for superfluidity of ultracold fermions in an optical lattice. *Nature* **443**, 961 (2006).
- Gericke, T. et al. Adiabatic loading of a Bose-Einstein condensate in a 3D optical lattice. *J. Mod. Opt.* **54**, 735 (2007).
- Xu, K. et al. Sodium Bose-Einstein condensates in an optical lattice. *Phys. Rev. A* **72**, 043604 (2005).

Acknowledgements

We thank the National Science Foundation and the Noble Foundation for financial support.

Author contributions

The experimental measurements and data analysis were carried out by J.O.A., Z.C., and Z.N.S. Theoretical analysis was performed by K.W.M. All authors discussed the results and contributed to the paper. All work was supervised by Y.L.

Competing interests

The authors declare no competing interests.

Additional information

Supplementary information The online version contains supplementary material available at <https://doi.org/10.1038/s42005-021-00562-y>.

Correspondence and requests for materials should be addressed to Y.L.

Reprints and permission information is available at <http://www.nature.com/reprints>

Publisher's note Springer Nature remains neutral with regard to jurisdictional claims in published maps and institutional affiliations.



Open Access This article is licensed under a Creative Commons Attribution 4.0 International License, which permits use, sharing, adaptation, distribution and reproduction in any medium or format, as long as you give appropriate credit to the original author(s) and the source, provide a link to the Creative Commons license, and indicate if changes were made. The images or other third party material in this article are included in the article's Creative Commons license, unless indicated otherwise in a credit line to the material. If material is not included in the article's Creative Commons license and your intended use is not permitted by statutory regulation or exceeds the permitted use, you will need to obtain permission directly from the copyright holder. To view a copy of this license, visit <http://creativecommons.org/licenses/by/4.0/>.

© The Author(s) 2021